



LAWRENCE
LIVERMORE
NATIONAL
LABORATORY

General Corrosion and Passive Film Stability

FY05 SUMMARY REPORT

*Suvasis Dixit, Sarah Roberts, Ken Evans, Tom
Wolery and Susan Carroll¹*

*Yucca Mountain Project
Lawrence Livermore National Laboratory*

July 7, 2006

¹ Corresponding author: carroll6@llnl.gov

Disclaimer

This document was prepared as an account of work sponsored by an agency of the United States Government. Neither the United States Government nor the University of California nor any of their employees, makes any warranty, express or implied, or assumes any legal liability or responsibility for the accuracy, completeness, or usefulness of any information, apparatus, product, or process disclosed, or represents that its use would not infringe privately owned rights. Reference herein to any specific commercial product, process, or service by trade name, trademark, manufacturer, or otherwise, does not necessarily constitute or imply its endorsement, recommendation, or favoring by the United States Government or the University of California. The views and opinions of authors expressed herein do not necessarily state or reflect those of the United States Government or the University of California, and shall not be used for advertising or product endorsement purposes.

Auspices

This work was performed under the auspices of the U.S. Department of Energy by University of California, Lawrence Livermore National Laboratory under Contract W-7405-Eng-48.

1. ABSTRACT	1
2. INTRODUCTION	1
3. METHODS	3
3.1. Materials.....	3
3.2. Autoclave Experiments	4
3.3. Analyses	5
3.4. Geochemical Calculations.....	6
4. RESULTS	7
4.1. Localized Corrosion.....	7
4.1.1. Liquid-Immersed Specimens.....	7
4.1.2. Vapor-Exposed Specimens.....	10
4.2. General Corrosion and Passive Film Composition and Thickness	12
4.2.1. Liquid-Immersed Specimens.....	13
4.2.2. Vapor-Exposed Specimens.....	17
5. DISCUSSION.....	20
5.1. General Corrosion at High Temperature in High Nitrate Solutions	20
5.2. Localized Corrosion.....	21
5.2.1. Summary of waste package outer barrier localized corrosion model.....	22
5.2.2. Is localized corrosion an artifact of the experimental protocol?	23
5.2.3. Role of nitrate on Alloy 22 localized corrosion at high temperature.....	25
6. SUMMARY: RELEVANCE OF AUTOCLAVE RESULTS TO CORROSION OF ALLOY 22 IN DUST DELIQUESCENT ENVIRONMENTS	27
7. REFERENCES	28
8. APPENDIX: LONG-TERM CORROSION TEST FACILITY.....	31

1. Abstract

We have studied Alloy 22 corrosion and passive film stability in nitrogen-purged Na-K-Cl-NO₃ brines having NO₃:Cl ratios of 7.4 at 160°C and NO₃:Cl ratios of 0.5 and 7.4 at 220°C in autoclave experiments under a slight pressure. The experiments were done to show the effect of high nitrate brines on the durability of the Alloy 22 outer barrier of the waste canisters. Ratios of NO₃:Cl used in this study were lower than expected ratios for the repository environment at these temperatures and atmospheric pressures (NO₃:Cl > 25), however they were thought to be high enough to inhibit localized corrosion.

Localized corrosion occurred on the liquid-immersed and vapor-exposed creviced specimens under all conditions studied. Crevice penetration depths were difficult to quantify due to the effects of deformation and surface deposits. Further characterization is needed to evaluate the extent of localized corrosion. The bulk of the surface precipitates were derived from the partial dissolution of ceramic crevice formers used in the study. At this time we do not know if the observed localized corrosion reflects the corrosiveness of Na-K-Cl-NO₃ solutions at elevated temperature over nine months or if it was an artifact of the experimental protocol. Nor do we know if much more concentrated brines with higher NO₃:Cl ratios formed by dust deliquescence will initiate localized corrosion on Alloy 22 at 160 and 220°C. Our results are consistent with the conclusion that nitrate concentrations greater than 18.5 molal may be required to offset localized corrosion of Alloy 22 at 160 and 220°C.

Stability of the passive film and general corrosion were evaluated on the liquid-immersed and vapor-exposed non-creviced specimens. Elemental depth profiles of the vapor-exposed specimens are consistent with the development of a protective Cr-rich oxide near the base metal. The combined passive film and alloy oxide of the immersed specimens was much thicker than for the vapor-exposed specimens. This may be attributed to the inability to transport reactants away from the surface with limited amount of fluid in the condensate compared to the large reservoir for the liquid-immersed specimens. Elemental depth profiles of the liquid-immersed specimens suggest that Cr(III) and Mo(II) in the passive film are oxidized to Cr(VI) and Mo(VI) and are dissolved in the high nitrate brines, because the alloy oxide layers were enriched with Ni relative to Cr and Mo in the base metal. An alumino-silicate-chloride precipitate was identified on specimens immersed in solutions with a NO₃:Cl ratio of 0.5 at 220°C. Further characterization is needed to identify all secondary phases. The inability to extract reliable rates from weight loss measurements suggests that other techniques are needed to evaluate long-term general corrosion of Alloy 22.

2. Introduction

Yucca Mountain, Nevada is the designated geologic repository for permanent disposal of high-level nuclear waste. Current waste package design calls for double-walled containers with an inner wall of stainless steel and an outer wall of a highly corrosion resistant Ni-Cr-Mo alloy (Alloy 22, N06022), which are protected with overlying titanium “drip shields” to prevent rocks and seepage water from contacting the containers (Gordon et al., 2002). Of concern are the corrosion resistance and long-term

integrity of these metal barriers. If the Yucca Mountain site license is approved, the waste packages will be placed in tunnels several hundred meters below the ground surface in partially saturated volcanic tuff, but still well above the groundwater table. A potential source of brines that may corrode metal containers and drip shields is the absorption of water by hygroscopic salts found in local and regional dust that will be deposited on metal surfaces during the repository construction and ventilation stages.

Recent experimental work has shown that mixtures of NaCl, KNO₃, NaNO₃ and/or Ca(NO₃)₂ salts form concentrated nitrate brines at very low relative humidity and high temperature (Carroll et al., 2005a,b). Mixtures of NaCl, KNO₃, NaNO₃ and/or Ca(NO₃)₂ are predicted to be the key salts that will control brine chemistry due to dust deliquescence (BSC 2004a, 2005). The discovery of the possibility of high temperature brine raised the concern for corrosion in the first 1000 – 2000 years, where temperatures are high and existing corrosion data are limited. The Yucca Mountain Project responded to the lack of corrosion data for Alloy 22 in K-Na-Cl-NO₃ brines at high temperatures by conducting short-term polarization experiments (Felker et al., 2006), performing long-term passive experiments (this study), and issuing the *Analysis of Dust Deliquescence for FEP Screening* report (BSC 2005). The screening report addresses the likelihood of localized corrosion of Alloy 22 utilizing the following decision tree:

1. Can multi-salt deliquescent brines form at elevated temperatures?
2. If brines form at elevated temperature, will they persist?
3. If brines persist, will they be corrosive?
4. If potentially corrosive brines form, will they initiate localized corrosion?
5. Once initiated, will localized corrosion penetrate the waste package outer barrier?

This decision tree provides a multi-layered argument in which answers to all of the questions must be “yes” in order for dust deliquescence to compromise the waste package outer barrier (2-cm thickness of Alloy 22). This report and Felker et al. (2006) present new experimental data that can be used to help answer the last three questions, which bear on the corrosiveness of deliquescent brines and the durability of the outer metal barrier of the waste canisters at temperatures from 110 to 220°C. A companion report on the deliquescence of NaCl-KNO₃-NaNO₃ and NaCl-KNO₃-NaNO₃-Ca(NO₃)₂ salt mixtures addresses the first two questions (Carroll et al., 2005b).

Here we report general and localized corrosion results of creviced and non-creviced Alloy 22 specimens that were immersed in brines having NO₃:Cl ratios of 7.4 at 160°C and NO₃:Cl ratios of 0.5 and 7.4 at 220°C for about nine months in static experiments. The creviced specimens were included to test the hypothesis that nitrate inhibits localized corrosion of Alloy 22 in brines with NO₃:Cl ≥ 0.5 at high temperature, as has been observed for Alloy 22 from 60 to 100°C in Na-K-Cl-NO₃ brines and from 100 to 150°C in Ca-Cl-NO₃ brines using electrochemical techniques (Ilevbare et al., 2005; Ilevbare et al., 2006). The limited number of tests conducted in FY05 were a follow-on study to Alloy 22 general corrosion experiments conducted from 120 to 220°C as a function of time over a range of NO₃:Cl (Orme et al., 2005), where solution compositions were based on knowledge of measured brine compositions at 120°C (Carroll et al., 2005). The experiments were not designed to mimic the very high nitrate brines expected for the

in-drift environment at peak temperatures and atmospheric pressure, where it is now known that brines can have $\text{NO}_3 = 100$ molal and $\text{NO}_3:\text{Cl} > 25$ at 160°C (Felker et al, 2006). Presumably, NO_3 concentrations and $\text{NO}_3:\text{Cl}$ ratios would be even higher at 220°C and atmospheric pressure. Additionally we review the status of on going experiments in the *Long-Term Corrosion Test Facility* at Lawrence Livermore National Laboratory.

3. Methods

3.1. Materials

All solutions were synthesized from reagent grade chemicals and deionized water. The solutions were high ionic strength brines containing Na, K, Cl, and NO_3 at 160 and 220°C (Table 3.1). The environments were designed to extend corrosion data for the $\text{NO}_3:\text{Cl}$ ratios studied by Orme et al (2005). For practical reasons, all solutions were undersaturated with respect to the solid salts at 90°C , so that the autoclaves could be loaded by pouring in fully mixed solutions under atmospheric pressure. Because the relevant solubility of chloride-nitrate salt mixtures increases strongly with increasing temperature, solution compositions corresponding to saturation at the desired experimental temperatures could not be prepared at lower temperature.

Table 3.1. Environmental conditions and identification numbers of specimens autoclaved for 267 days and evaluated by XPS and Auger.

Temperature (°C)	$\text{NO}_3:\text{Cl}$	NaCl molal	NaNO_3 molal	KNO_3 molal	Total Molal	Liquid/Vapor	XPS and Auger Specimen ID
160	7.4	2.5	3.4	15.1	21	Liquid	JE1307, JE1316
160	7.4	2.5	3.4	15.1	21	Vapor	JE1304, JE1329
220	7.4	2.5	3.4	15.1	21	Liquid	JE1302, JE1312
220	7.4	2.5	3.4	15.1	21	Vapor	JE1339, JE1310
220	0.5	6.4		3.2	9.6	Liquid	JE1323, 1309
220	0.5	6.4		3.2	9.6	Vapor	JE1313, JE1301

Annealed Alloy 22 foil specimens were used to measure general corrosion rates by weight loss; creviced-foil specimens were used to evaluate localized corrosion by secondary electron microscopy, energy dispersive spectroscopy, and vertical scanning interferometry. Chemical and microscopic analyses of non-reacted foils yield no unusual chemistry or grain structures. All foil specimens were about 2 cm in diameter and 51 microns thick. Non-creviced foils from similar tests (Orme et al., 2005) were used in the FY05 tests after they were polished with a 3-micron diamond paste to remove alloy-oxide layers on the surface. Note that the only non-creviced specimens were used in the previous tests and the reacted foils were not coated with aluminum hydroxide precipitates. We do not believe that re-polishing the samples affected the structure or the composition of the surface, but it was not explicitly measured. The creviced-specimens had an as-received surface finish and had not been previously tested. Crevice formers were attached by tightening the crevice former bolts to a torque of 70 in-lb. The ceramic crevice formers consisted of aluminum and oxygen as identified by energy dispersive spectroscopic analysis and were the main source of aluminum for the precipitates. Some

of the crevice formers may have been made of mullite ($\text{Al}_6\text{Si}_3\text{O}_{15}$) and provided some aluminum and silica for the precipitates, however this was not confirmed.

3.2. Autoclave Experiments

The 2 L (liter) autoclaves used in this study are made of Hastelloy C-276, which is composed of the same chemical elements as Alloy 22 and has a comparable corrosion resistance to Alloy 22 in near neutral pH solutions (Rebak 2000). A specimen holder made of Alloy 22 was used inside each autoclave. The similar compositions of autoclave and specimen holder prevent contamination by “foreign” chemical elements and reduce galvanic coupling between specimen and holder. The Alloy 22 specimens were not electrically isolated from the Hastelloy C-276 autoclave. Specimens were held in a vertical position to minimize settling of secondary precipitates on the Alloy 22 specimens.

To assemble each experiment, 1 L of brine solution was added to the autoclave at 90°C. The assembled specimen holder was then put in the autoclave, such that half the foils and pucks were fully immersed in liquid and the other half were fully exposed to the vapor phase above the liquid¹. The autoclave was then sealed and the solution was purged with nitrogen for one hour at 100°C to remove oxygen and carbon dioxide gases. This purging was done to facilitate comparing the results with those from electrochemical Alloy 22 corrosion tests that were performed in nitrogen-purged environments. At high temperatures and high nitrate concentrations, nitrate will be the most readily available oxidant for Alloy 22 corrosion. However, in the fully aerated repository conditions oxygen will also be present as an oxidant and may affect the stability of the passive film. After purging, the autoclaves were brought to run temperature and reacted for 267 days (\approx 9 months). The autoclave pressure reflects the vapor pressure generated by the brine at the run temperature². Any salt that precipitated when the solution was purged was expected to re-dissolve at run temperature and pressure.

After about 9 months of reaction, autoclave temperature and pressure were reduced to ambient values, and specimen holders were removed. Crevice formers were detached from relevant specimens, and all foils and pucks were rinsed with de-ionized water multiple times to remove any residual salts that precipitated on the specimens when the autoclaves cooled. Verification of removal of salts visually with an optical microscope was sufficient to ensure that the salts were removed. Removal of salts with a non-aggressive solution, such as water, was the first step in cleaning the specimens for weight loss and surface analyses.

¹ Each autoclave contained 2 pucks, 6 non-creviced foils, and 4 creviced foils exposed to the vapor and 2 pucks, 6 non-creviced foils, and 6 creviced foils fully immersed in the solution.

² Experimental pressures are estimated to be 6 atmospheres at 160°C and 23 atmospheres at 220°C based on water vapor pressure (Weast and Astle, 1981). Actual pressures may be lower because the concentrated solutions will lower the activity of water and the corresponding pressure of the system.

3.3. Analyses

General corrosion rates were determined from the area, density, and weight difference of the non-creviced foils prior to reaction and after acid treatments to remove the aluminum hydroxide precipitates and the alloy oxide alteration layer from the foil surface using the ASTM-G1-03 C6.1 method (See DTN LL050903312251.149 for details). Intermediate weights were measured after individual washes with deionized water and the acid cleaning solutions. All foil weights were measured in triplicate. Specimens were cleaned in two solutions: 150 ml of 37% HCl in 1000 ml H₂O and 100 ml 95% H₂SO₄ in 1000 ml H₂O. The weight-loss method assumes that the cleaning solutions selectively dissolve oxides but do not dissolve the base metal. A polished foil was included for each set of specimens as a control to measure loss of base metal in the cleaning process. Each specimen set was then sequentially treated with cleaning solutions and weighed. Complete removal of all oxide layers is indicated when additional cleaning treatments yield no incremental loss of weight. At the time of writing this report, liquid-immersed foils had been acid washed up to 32 times and vapor-exposed foils had been acid washed up to 14 times. The uncertainty shown in the plots is the standard deviation for the weight loss for each specimen set; this is greater than the measurement error (± 0.000007 grams).

Oxide layer composition developed as a product of general corrosion was determined using x-ray photoelectron spectroscopy (XPS) and Auger electron spectroscopy (AES) depth profiling on the reacted puck specimens. Puck specimens were simply washed with deionized water to remove salts prior to analysis (no acid washes). XPS is a surface-sensitive analysis method that as used here measures the elemental composition and the chemical state of oxides formed on Alloy 22 pucks over a large (mm²) area but for a shallow depth (nm). Photoelectrons are generated within the x-ray penetration depth (typically many microns), but only the photoelectrons within the top three-photoelectron escape depths are detected. Escape depths are on the order of 15–35 Å, which leads to an analysis depth of ~50–100 Å. Typically, 95% of the signal originates from within this depth. All XPS measurements were performed on a PHI Quantum 2000 Quantum Scanning ESCA Microprobe using a monochromatic Al K_a source with photon energy of 1486.6 eV. The analysis area was 1400 μm × 300 μm. Spectra were charge-corrected by aligning the chromium Cr2p₃ peak at 577.0 eV or the carbon C1s peak at 284.8 eV. Details of the results can be found in Charles Evans reports (DTN LL050903312251.149).

Auger depth profiling was used to obtain elemental composition through the outer oxide layers to the base metal. All Auger measurements were performed using a Physical Electronics (PHI) 680 Scanning Auger Microprobe. Depth profiles were obtained by alternating an acquisition cycle with a sputter cycle. During the acquisition cycle, selected elemental peak intensities were collected. The sputter cycle removed material from the surface of the specimen using a 5-keV Ar⁺ source rastered over a 2-mm × 2-mm area. In order to eliminate crater wall effects, data was acquired from a smaller region in the center of the sputtered area. The depth profiles acquired show the etch time on the x-axis. The ion gun conditions were chosen to be consistent with an etch rate of 5.7 nm/min on a thermally grown silicon dioxide reference material (“SiO₂-equivalent depths”). Different materials will etch at different rates dependent on surface topography,

crystallographic orientation, and incident ion-beam angle. Details of the results can be found in Charles Evans (2005b).

Crevice-foil specimens showed significant oxide precipitation under the crevice teeth. Secondary electron microscopy was used to image crevice corrosion and secondary precipitates using an FEI Company Quanta 200 Environmental SEM with an Everhart-Thornley (secondary electron) detector, an accelerating voltage of 20kV, and a beam current of a $100\mu\text{A}$, and magnifications ranging from 50x to 5000x. Chemical information was obtained using an EDAX Genesis Energy Dispersive Spectroscopy (EDS) system, with accelerating voltages ranging between 20 and 30kV depending on the regions observed. The EDS analyses are semi-quantitative and are used as chemical fingerprints to identify the composition of secondary precipitates. In many cases, EDS spectra reflect the combined composition of the precipitates and the base metal, because the electron beam penetrates beyond the precipitates.

Crevice corrosion was visually identified as etched metal using a Zeiss optical microscope to 10x magnification. For select specimens crevice corrosion topography was imaged using vertical scanning interferometry (VSI) with a Wyko NT3300 system. It employs non-contact optical interferometry to measure surface roughness and obtain a surface height profile with a vertical resolution to $\pm 1\text{nm}$. The VSI data presented in the present report should be considered as preliminary.

3.4. Geochemical Calculations

We use the EQ3/6 geochemical code (Wolery and Jarek, 2003) and the Yucca Mountain Project high-temperature Pitzer model (BSC, 2004b) to calculate brine pH, $p\text{HCl}(\text{g})$ and $p\text{HNO}_3(\text{g})$ in the vapor phase, and condensate pH, $[\text{Cl}^-]$, and $[\text{NO}_3^-]$ to constrain the interpretation of the localized corrosion observed in the creviced samples (Table 3.2). We equilibrate brines and condensates with boehmite (γAlOOH_s) to account for the observed aluminum hydroxide precipitates in the creviced specimens, because this is predicted to be the stable aluminum hydroxide³. Reaction pressure was allowed to vary by means of the 1.013-bar/steam-saturation curve. The Pitzer model is based on the available experimental data and includes binary interactions ($\beta_{\text{M,X}}^{(0)}$, $\beta_{\text{M,X}}^{(1)}$, $\beta_{\text{M,X}}^{(2)}$, $C_{\text{M,X}}^\phi$) between two different kinds of ions of opposite charge (cation M and anion X), and also binary ($\theta_{\text{M,M'}}$, $\theta_{\text{X,X'}}$) interactions between ions of like charge and ternary interactions ($\psi_{\text{M,M',X}}$, $\psi_{\text{X,X',M}}$) involving three ions in common-anion and common-cation ternary systems to account for the non-ideal behavior of the brine solutions (cf. Pitzer, 1991). It should be noted that we are using the Pitzer model beyond its validation temperature of 140°C . We suspect that actual brine pH, a_{Cl^-} and $a_{\text{NO}_3^-}$ are different because the model uses constant K- NO_3 interaction parameters that do not capture increase in solubility at higher temperatures. Changes in brine pH, a_{Cl^-} and $a_{\text{NO}_3^-}$ will propagate to condensate pH, $[\text{Cl}^-]$, $[\text{NO}_3^-]$ and $p\text{HCl}(\text{g})$ and $p\text{HNO}_3(\text{g})$ values. As such calculated values should only be used to indicate qualitative trends within the autoclave experiments.

³ Aluminum-silicates and alloy metal oxides were not included in the calculation, because they were much less abundant than the aluminum oxide/hydroxides and should have a minimal impact on the bulk $p\text{HCl}(\text{g})$ and $p\text{HNO}_3(\text{g})$.

Table 3.2 EQ3/6 calculations of the brine pH and Al, vapor phase $p\text{HCl(g)}$ and $p\text{HNO}_3\text{(g)}$, and condensate pH, Al, Cl, and NO_3 to constrain the interpretation of the localized corrosion observed in the creviced samples. Superscripts tie brine chemistry to condensate chemistry.

T°C	pH (NBS)	log $p\text{HCl(g)}$	log $p\text{HNO}_3\text{(g)}$	Al m	NO_3 m	Cl m	$\text{NO}_3\text{:Cl}$
Brines							
160 ¹	6.06	-7.84	-8.53	0.0001	18.5	2.5	7.40
220 ²	6.29	-6.66	-7.44	0.0009	18.5	2.5	7.40
220 ³	5.94	-5.88	-7.03	0.0002	3.2	6.4	0.50
Condensates							
160 ¹	2.95	-7.84	-8.53	3×10^{-6}	0.0004	0.0008	0.51
220 ²	3.10	-6.66	-7.44	4×10^{-7}	0.0003	0.0005	0.56
220 ³	2.76	-5.88	-7.03	1×10^{-6}	0.0004	0.0015	0.24

4. Results

4.1. Localized Corrosion

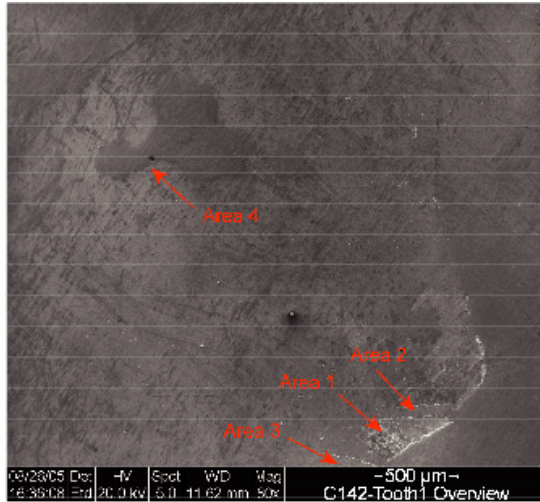
In this report localized corrosion refers to corrosion that occurs within occluded area formed by a ceramic crevice former and Alloy 22 metal foil. Localized corrosion was observed on specimens immersed in the solution and on specimens held in the vapor phase at all conditions studied (160°C with $\text{NO}_3\text{:Cl} = 7.4$; 220°C with $\text{NO}_3\text{:Cl} = 0.5$ and 7.4). This corresponds to a total of 432 creviced areas for specimens immersed in solutions and 288 creviced areas for specimens suspended in the vapor phase above those solutions⁴. The extent of corrosion varied from tooth to tooth at all conditions studied, but was typically concentrated at the root and the edges of the crevice former tooth. (see DTN LL050903312251.149 for optical images). Localized corrosion was accompanied by precipitation of secondary aluminum hydroxides⁵ and corrosion products.

4.1.1. Liquid-Immersed Specimens

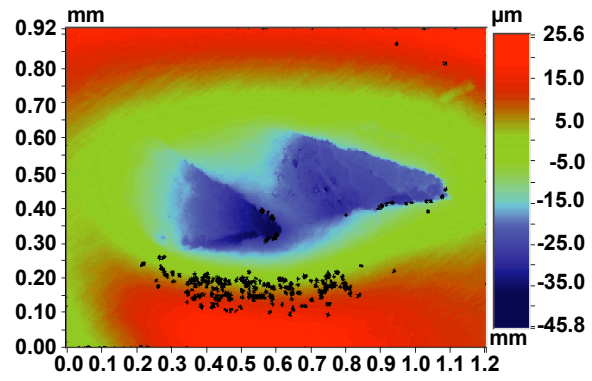
Figures 4.1a-e shows a series of SEM photomicrographs, EDS spectra, and interferometry images underneath one tooth of a creviced Alloy 22 specimen that was immersed in a 21 molal Na-K-Cl- NO_3 brine ($\text{NO}_3\text{:Cl} = 7.4$) at 220°C for about nine months. Similar features were observed for creviced specimens immersed in solutions at 160°C with $\text{NO}_3\text{:Cl} = 7.4$ and at 220°C with $\text{NO}_3\text{:Cl} = 0.5$ (see DTN LL050903312251.149 for SEM images and EDS spectra). There are two kinds of

⁴ An assembled creviced specimen contains 24 creviced areas. Each autoclave contained 6 creviced specimens immersed in the aqueous solution and 4 creviced specimens suspended in the vapor phase, for a total of 720 creviced areas in three autoclave experiments.

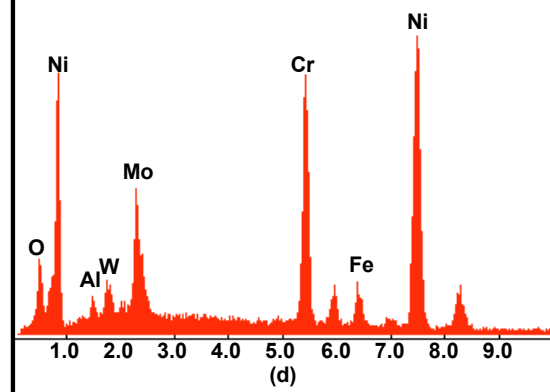
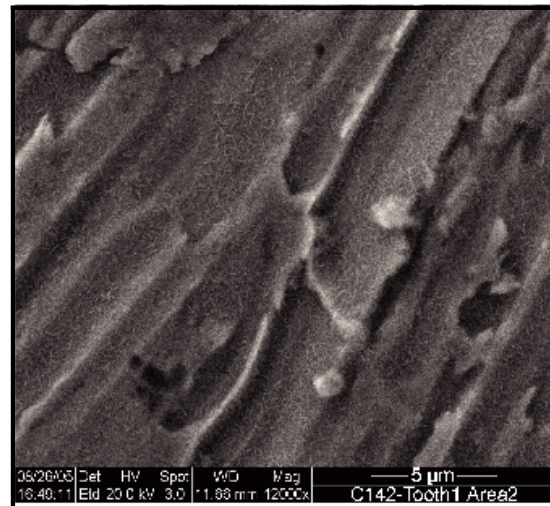
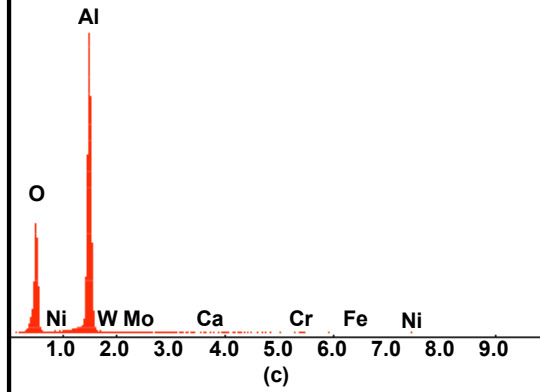
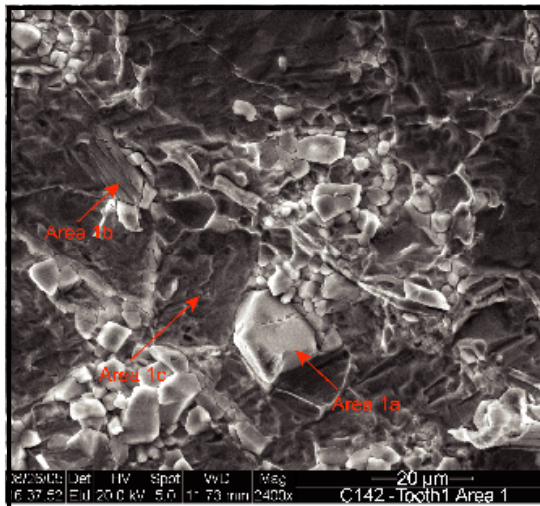
⁵ We refer to non-alloy oxides collectively as aluminum hydroxides, because the bulk of the precipitates are estimated to be boehmite ($\gamma\text{-AlOOH}$), even though some silica was also detected in the surface analysis of reacted non-creviced specimens.



(a)



(b)



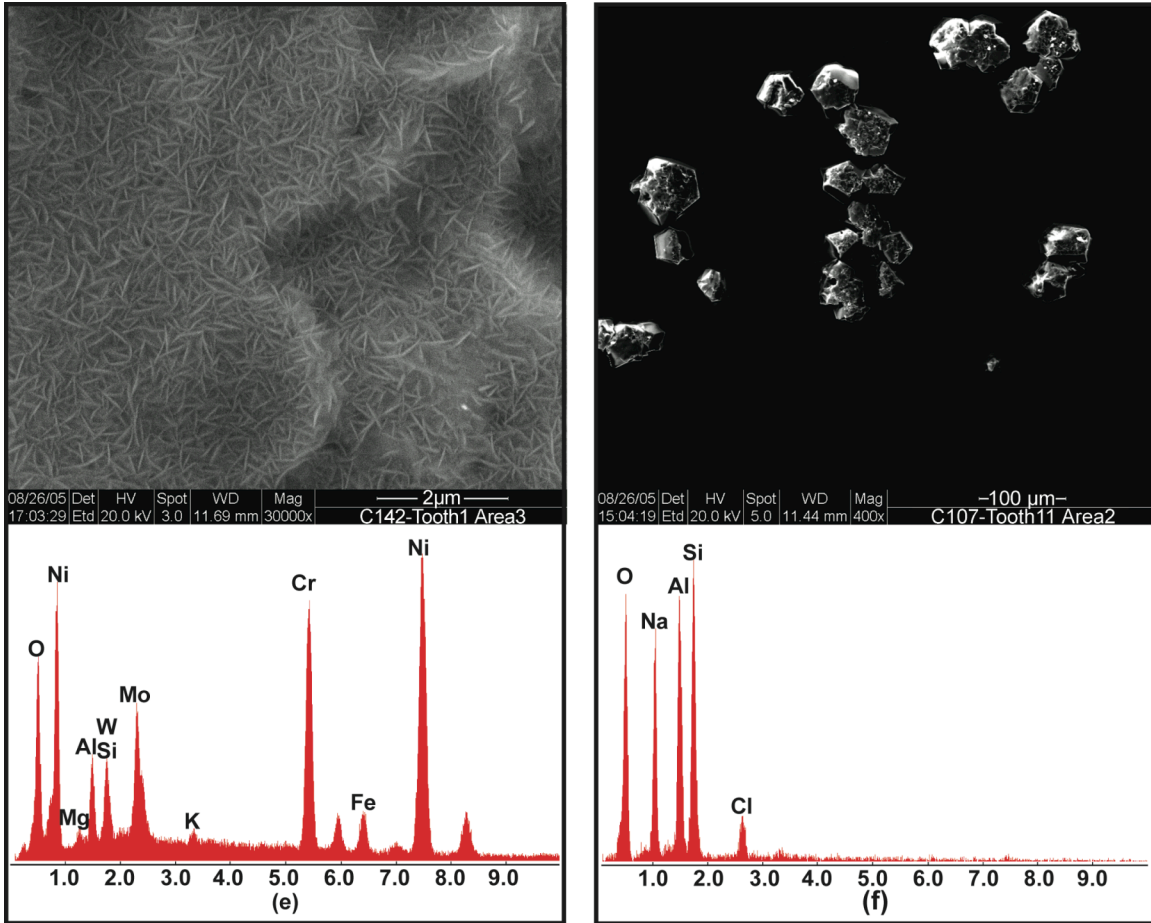


Figure 4.1. Crevice corrosion of Alloy 22 immersed in Na-K-Cl-NO₃ brines at 220°C with NO₃:Cl = 7.4 (C142, tooth 1; a-e) and NO₃:Cl = 0.5 (C107, tooth 11; f): (a) SEM overview (b) interferometry image of corrosion pits foils at tooth root (Area 1), (c) SEM image of Area 1 and EDS spectra of aluminum hydroxide precipitates, (d) corroded surface in Area 2, (e) corrosion produced in Area 3 under the crevice tooth, and (f) chloride-containing aluminosilicate.

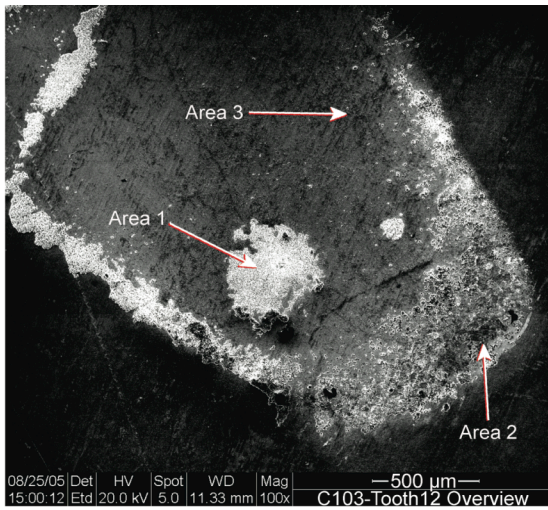
secondary oxide precipitates under the ceramic crevice formers. Aluminum hydroxide precipitates are present as large islands in the middle of the tooth area and also on the edges, as well as single crystals within corroded areas at the tooth root (Figure 4.1a,c). The second type of precipitate is an oxide corrosion product from the base metal, which forms a sub-micron, needle-like habit directly on the corroded surface at the tooth root (Figure 4.1d) and other less corroded areas within the tooth (Figure 4.1e). We use the EDS spectra as qualitative fingerprints of the composition of the oxides. The aluminum hydroxide (2-3 microns in diameter) is clearly identified by a spectra where the aluminum peak is about two times the intensity of the oxygen peak. The second kind of precipitate consists of much smaller corrosion products (submicron in length) with EDS spectra showing contributions from both the oxide and the base metal, as well as some aluminum hydroxide. We identify these oxides as corrosion products even though there is some aluminum because the spectrum is not a representative fingerprint of the

aluminum hydroxide (Fig. 4.1c: the aluminum peak is less intense than the oxygen peak). Therefore, corrosion products must contribute to the total oxygen signal. We cannot determine the composition of the corrosion products because the base metal contribution cannot be subtracted from the spectra. An aluminosilicate with chloride was observed only in the experiments at 220°C with $\text{NO}_3:\text{Cl} = 0.5$ (Figure 4.1f) in addition to the aluminum hydroxide and corrosion product oxides. Possible phases include sodalite, cancrinite, and scapolite (Deer et al., 1992).

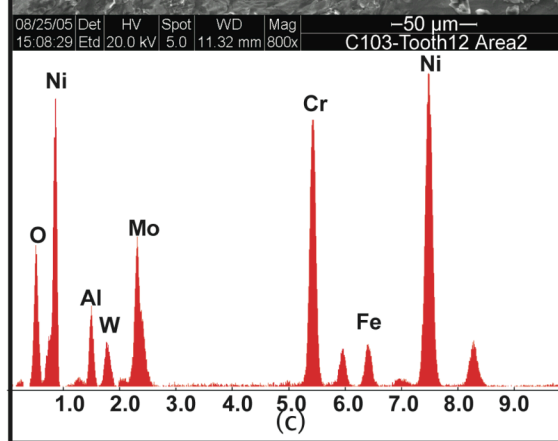
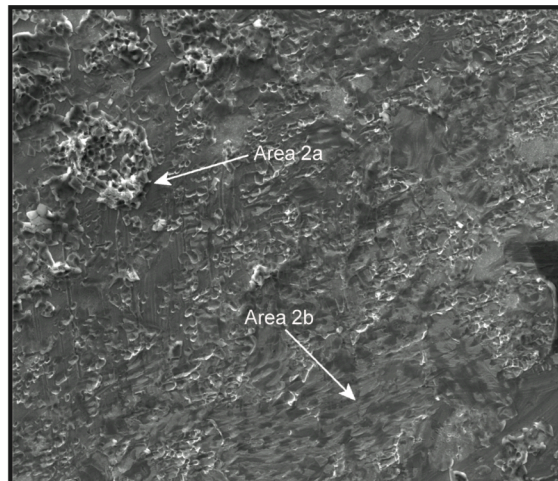
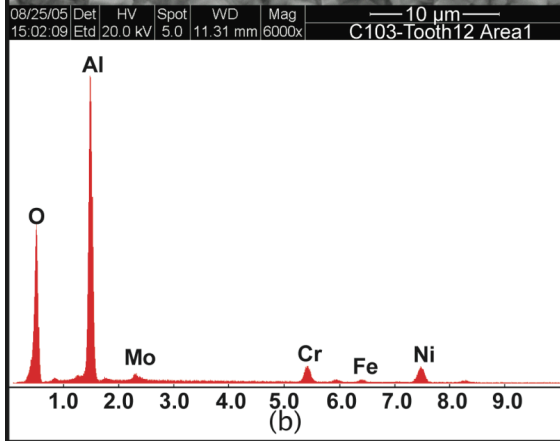
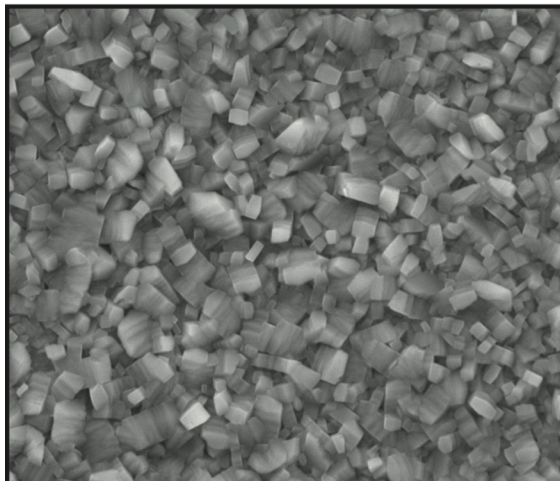
Interferometry was used to measure the corrosion depth in the creviced area on select teeth (one per experiment). Figure 4.1b shows two geometric areas in a tooth root (immersed specimen C142, 220°C, $\text{NO}_3:\text{Cl} = 7.4$). The topographic relief from high to low is about 45 microns. The extent of crevice corrosion may span less than 45 microns, because secondary precipitates have not been removed from the surface and the foil, and because the measurement may also reflect deformation of the foil. The crevice corrosion shown here is one of the more extensive examples. Other surfaces studied with vertical scanning interferometry showed topographic relief from 3 to 30 microns. See DTN LL051001412251.156 for these images. Note that only a few of the specimens were analyzed using interferometry. A systematic analysis of all creviced areas would be required to fully evaluate the extent of localized corrosion.

4.1.2. Vapor-Exposed Specimens

Figure 4.2 shows a series of SEM photomicrographs and EDS spectra underneath one tooth of a creviced Alloy 22 specimen that was suspended in the vapor phase above a 9.6 molal Na-K-Cl- NO_3 brine ($\text{NO}_3:\text{Cl} = 0.5$) at 220°C for about nine months. Similar features were observed for vapor-exposed creviced specimens at 160 and 220°C suspended above brines with $\text{NO}_3:\text{Cl} = 7.4$ (see DTN LL050903312251.149 for SEM images and EDS spectra). Similar to the immersed specimens, specimens suspended in the vapor phase contained both aluminum hydroxides and corrosion product oxides under the crevice formers. In general, aluminum hydroxide precipitation was more extensive in the vapor phase than in the liquid, presumably because there was not enough condensate to transport aluminum out of the creviced area. Figure 4.2a shows aluminum hydroxide precipitates in the middle and the edges of the tooth. In some cases the aluminum hydroxide completely covered the creviced area. Similar to the case for the immersed specimens, we infer precipitation of corrosion products from the EDS spectra taken in the corroded area near the tooth root (Figure 4.2c) from a less intense aluminum peak relative to the oxygen peak than was observed for aluminum hydroxide (Figure 4.1b). This requires that corrosion products contribute to the total oxygen signal. Total metal signals are a combination of the corrosion product and the base metal and cannot be separated into their individual components. In addition to crevice corrosion, general corrosion occurred in the vapor-exposed specimens, as is shown by the presence of alloy oxides between the two teeth shown in Figure 4.2d. In this case, we see only trace amounts of aluminum, indicating that the oxide is clearly a corrosion product. It was not possible to determine the penetration depth of localized corrosion in the base metal because extensive aluminum hydroxide precipitation masked corroded areas beyond the resolution of the interferometry technique. However, SEM images show corrosion of the base metal as etched surfaces in Figure 4.2c. Creviced foils will need to be cleaned in order to determine the extent of localized corrosion.



(a)



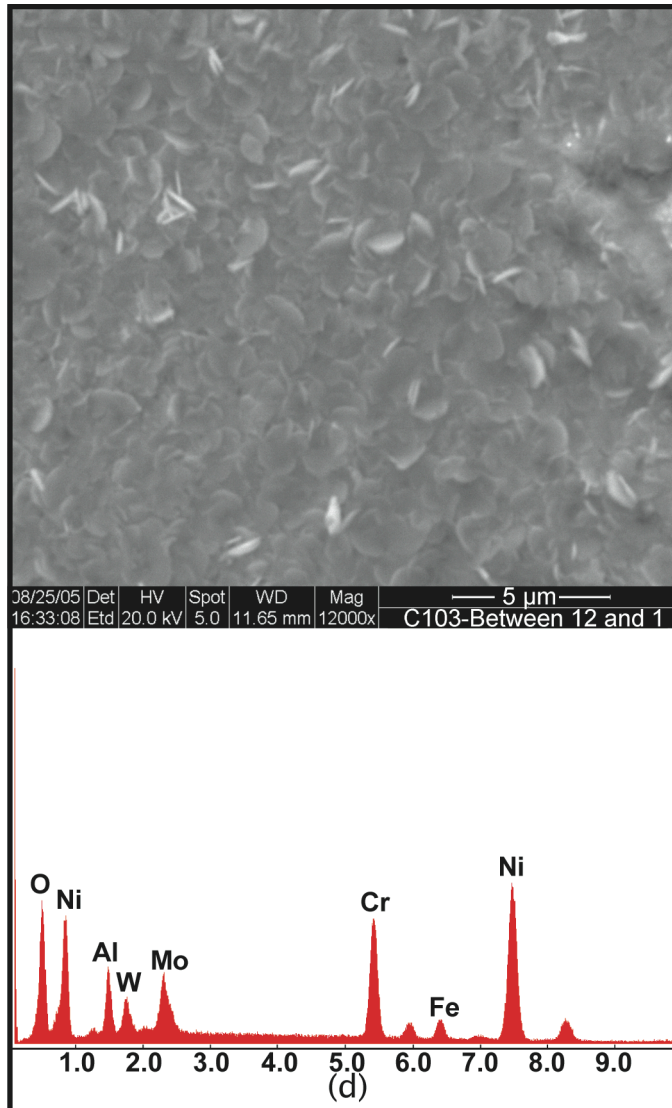


Figure 4.2. Crevice corrosion of Alloy 22 suspended in the vapor phase above Na-K-Cl-NO₃ brines at 220°C with NO₃:Cl = 0.5 (C103, tooth 12): (a) SEM overview (b) SEM image and EDS spectra of aluminum hydroxide precipitates in Area 1, (c) SEM image and EDS spectra of corrosion products in Area 2, and (d) SEM image of area between tooth 12 and 1 showing corrosion on non-occluded surface.

4.2. General Corrosion and Passive Film Composition and Thickness

This section discusses the oxides formed by reaction of the Na-K-Cl-NO₃ brines with Alloy 22 surface and geologic materials. The surface oxide layer consists of deposits of mainly an aluminum hydroxide, some silicate, and an alloy oxide that is enriched in Ni relative to Cr and Mo compared to the base metal composition. The alloy

oxide is about 10 times thicker in the liquid-immersed specimens compared to vapor-exposed specimens.

4.2.1. Liquid-Immersed Specimens

Alloy 22 metals in the outermost surface film were identified as primarily Ni and Cr oxides (1.5 to 3.5 nm, Table 4.1). Aluminum and silicon oxides were identified in addition to the alloy oxide components. The most abundant alloy constituent detected on all the specimens was Ni, followed by Cr. Some of the other alloy constituents (Mo, Fe and W) were not detected in many of the specimens. All of the specimens had a surface oxide primarily composed of Ni(OH)₂ (70–100%) followed by various chromium oxides (0–24%). Determination of speciation of Cr in the liquid-immersed specimens was not possible because the values were too low, due to the thick Al and Si coating on top of the alloy oxide layer formed by general corrosion. Thus we could not confirm the oxidation of Cr metal to Cr(VI) as was observed in previous experiments at 220°C, which did not contain a thick Al and Si coating (Orme et al., 2005).

Figure 4.3 shows the Auger depth profiles of the atom percent of the alloy metals (Me/(Ni+Cr+Mo+W+Fe)) and atom percent of Al + Si and O as a function of sputter time through the outer surface layer to the base metal. A significant amount of dissolved aluminum from the ceramic crevice formers and dissolved silica from an unknown source (possibly mullite crevice formers) precipitated on the non-creviced pucks. Comparison of Al+Si and O suggest that the bulk of the oxygen is associated with an aluminum hydroxide with some silicate. This is confirmed by constant ratio of Al+Si to O from the surface to the base metal. We infer that some oxygen is associated with the alloy metals forming an oxide enriched in Ni and depleted in Cr and Mo relative to the base metal (Figure 4.3a,c,e). The composition of the alloy oxide tends towards the composition of the base metal with depth. Almost equal concentration of Cr and Mo are found in the surface layers, however, the concentrations were about half of those of Ni. Almost no Fe or W, which are present at very low concentration in the base metal, was detected in the surface oxide layer. Calculation of the alloy oxide thickness is difficult in these specimens because aluminum hydroxide⁵ precipitation masks the location of the alloy oxide. Reasonable bounds for the alloy oxide composition are (1) alloy metal ratio in the base metal (constant value) and zero oxygen and (2) alloy metal ratios with Ni less than 1 in the outer surface layer, because Ni metal ratios equal to 1 are likely to correspond to Ni associated with the aluminum hydroxide. The boundaries are based on the assumption that no oxygen is present in the base metal and that Cr(VI) and Mo(VI) oxy-anions leached from the alloy oxide layers do not sorb onto the aluminum hydroxide that precipitated on the specimens.

The alloy oxide thickness, indicated by the length of the arrow on Figure 4.3, increases from 10 to 20 minutes from 160°C to 220°C when Alloy 22 was reacted in solutions with NO₃:Cl = 7.4. Thicker alloy oxides of 65 minutes formed when Alloy 22 was reacted in solutions NO₃:Cl = 0.5 at 220°C. We limit the

⁵ We refer to non-alloy oxides collectively as aluminum hydroxides, because the bulk of the precipitates are estimated to be boehmite (γ -AlOOH), even though some silica was also detected in the surface analysis of reacted non-creviced specimens.

Table 4.1: XPS results of the alloy oxide composition reported as atom percent.

Specimen	T (°C)	NO ₃ :Cl	Molal	Days	Envir.	Ni oxide	Cr oxide	Fe oxide	Mo oxide	W oxide	Ni/Cr oxide
JE 1304	160	7.4	21	240	Vapor	70.8	17.5	6.1	5.3	0.3	4.0
JE 1329	160	7.4	21	240	Vapor	73.2	16.7	5.3	4.5	0.3	4.4
JE 1307	160	7.4	21	240	Liquid	71.8	24.4	0.0	3.9	0.0	2.9
JE 1316	160	7.4	21	240	Liquid	46.0	44.8	0.0	9.2	0.0	1.0
JE 1313	220	0.5	9.6	240	Vapor	85.7	8.7	4.0	1.7	0.0	9.9
JE 1301	220	0.5	9.6	240	Vapor	83.7	9.3	4.1	3.0	0.0	9.0
JE 1323	220	0.5	9.6	240	Liquid	97.6	2.4	0.0	0.0	0.0	40.7
JE 1309	220	0.5	9.6	240	Liquid	96.7	3.3	0.0	0.0	0.0	29.3
JE 1339	220	7.4	21	240	Vapor	87.6	8.8	2.7	0.9	0.0	10.0
JE 1310	220	7.4	21	240	Vapor	76.5	16.3	3.8	3.3	0.1	4.7
JE 1302	220	7.4	21	240	Liquid	98.6	0.0	1.1	0.3	0.0	
JE 1312	220	7.4	21	240	Liquid	100.0	0.0	0.0	0.0	0.0	

examined thickness of the alloy oxide to 20 minutes at 160°C because oxygen values decrease to zero at shallower depths than those of the base metal surface; Ni-enriched layers in the absence of oxygen may indicate changes in the local composition. Our observations are consistent with those of Orme et al. (2005) who measured oxide thickness using cross-sectional TEM on Alloy 22 reacted at elevated temperature in various NO₃:Cl brines for about 9 months. Orme's experiments were conducted in the absence of crevice formers and were not complicated by precipitation of aluminum hydroxide. Orme found that the alloy oxide layer ranged from 0 to 60 nm when Alloy 22 was reacted at 140°C in solutions with NO₃:Cl = 0.05 and 0.5. This value is consistent with an alloy oxide layer of 57 nm calculated as SiO₂-equivalent depth when Alloy 22 was reacted at 160°C in solutions with NO₃:Cl = 0.5 in this study. When Alloy 22 was reacted at 220°C in solutions with NO₃:Cl = 0.3, the alloy oxide layer was 500 nm thick as measured by x-sectional TEM. This value is also consistent with 100 to 370 nm calculated as SiO₂-equivalent thick oxide layers in this study. Note that the use of SiO₂-equivalent thickness of the alloy oxide layer is for qualitative comparison only.

The weight loss measurements are summarized in Figure 4.4. All specimens show a measurable weight gain, which increases with increasing temperature. The bulk of the weight gain can be attributed to precipitation of secondary aluminum hydroxides from the ceramic crevices used to study localized corrosion.

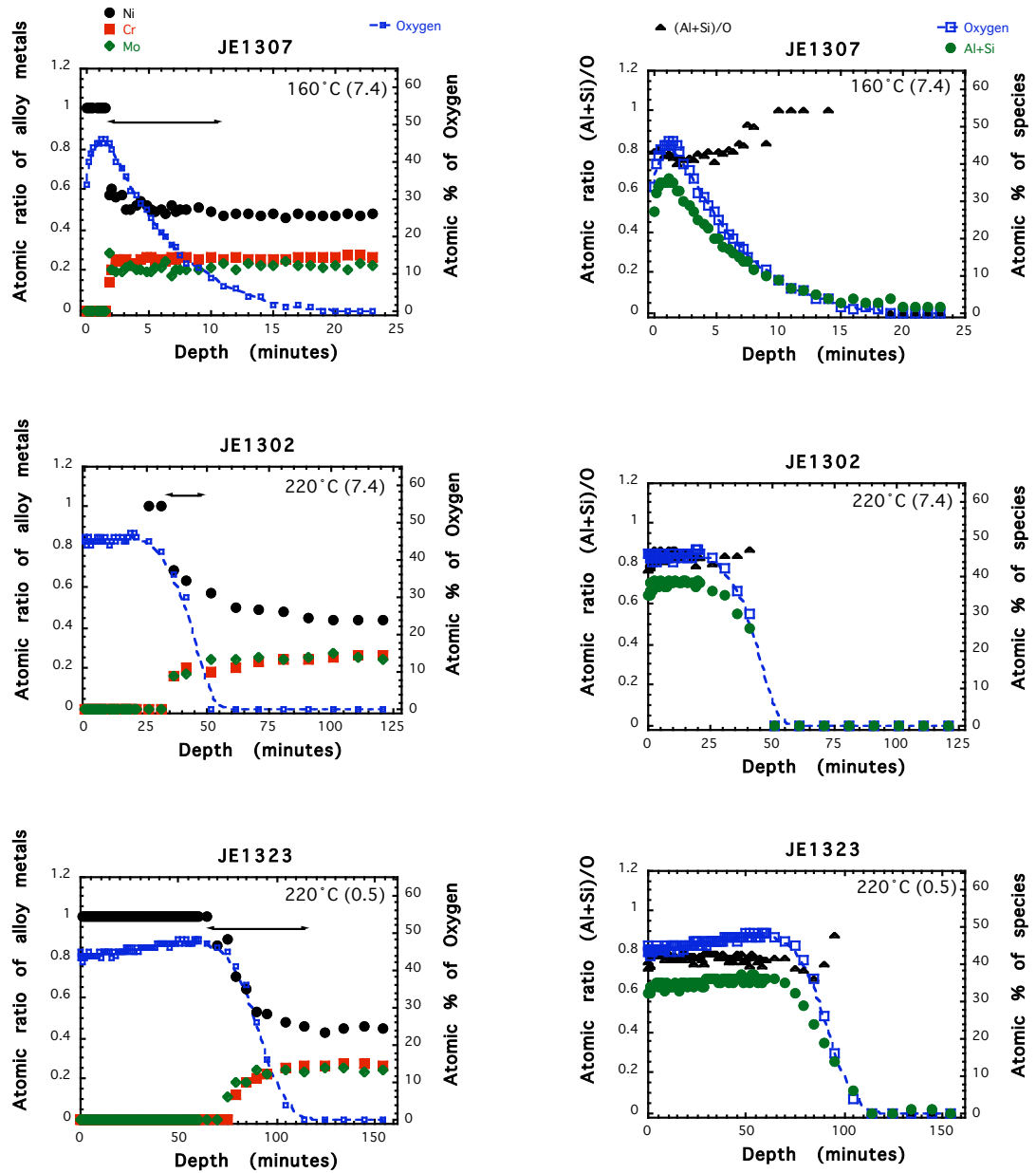


Figure 4.3: Auger depth profiles of liquid-immersed specimens autoclaved for nine months. Arrows indicate thickness (minutes sputtered) for the alloy oxide. Note the different scales on the two y-axis of each of the plots.

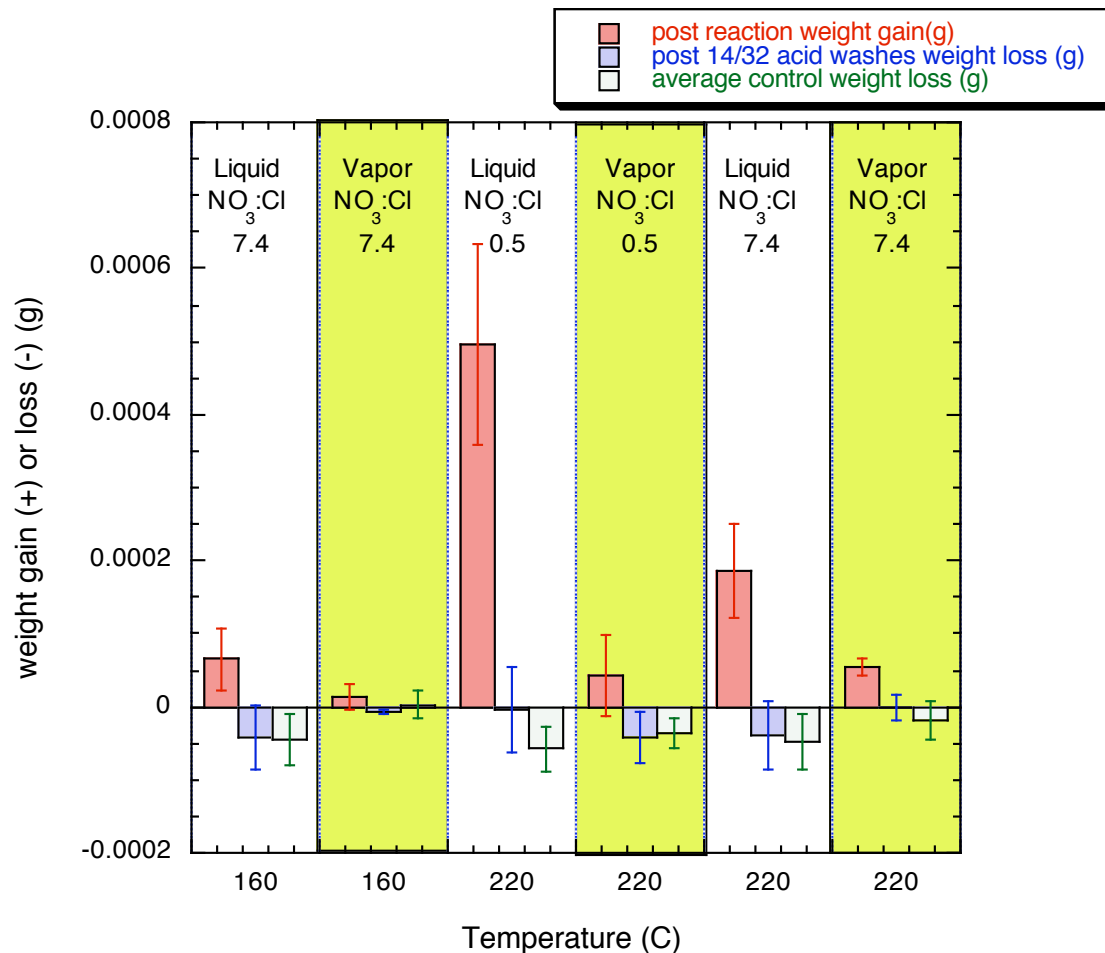


Figure 4.4. Gravimetric analysis of Alloy 22 immersed (liquid) in Na-K-Cl-NO₃ solutions with varying NO₃:Cl and suspended in the vapor phase above those solutions at 160°C and 220°C. Weight gain/loss after 9 months of reaction (water rinses to remove salts), after reacted foils were treated with 14 (vapor-exposed specimens) to 32 acid washes (liquid-immersed specimens) to remove oxides, and after non-reacted foils were treated with an equal number of acid washes as controls.

The resulting estimate (after 29 to 32 acid treatments) of near zero corrosion rates of 8 ± 12 nm/yr is not consistent with the thick alloy oxides inferred from the Auger depth profiles, suggesting that acid washes did not fully remove the oxide film (see DTN LL050903312251.149 for calculation of weight loss rates). Despite this observation, additional acid treatments were not performed because weight loss from the control indicated that base metal was compromised by the acid treatments. Thus it was not possible to distinguish between losses of oxide film from the base metal to calculate an accurate rate.

4.2.2. Vapor-Exposed Specimens

Similar to the liquid-immersed specimens, XPS analysis show that specimens in the vapor phase had a surface oxide primarily composed of $\text{Ni}(\text{OH})_2$ (70–90%) followed by various chromium oxides (8–24%) (Table 4.1, Figure 4.5). Figure 4.6 shows the contribution from various chromium species in the vapor phase specimens determined in this study and in a previous study of Alloy 22 general corrosion by Orme et al. (2005). The primary chromium oxides were identified as Cr_2O_3 and CrO_2 ; with minor amounts of CrO_3 . Cr metal was detected only at 140 and 160°C. Chemical state was assigned with non-linear least squares fit to the $\text{Cr}2p_{3/2}$ high-resolution spectra. Species shown below are those for which reference data were available and that correspond to the binding energies yielded from the curve fitting. It should be noted that for a given peak, a number of mathematically valid results may exist, therefore, the reported oxide distributions and concentrations may have relatively high uncertainty. The curve fits were included mainly to provide an estimate of alloy oxide(s) ratios and to identify potential oxide species where possible.

Alloy oxide film of Alloy 22 specimens suspended in the vapor phase above the Na-K-Cl- NO_3 solutions is much thinner than the film that formed on immersed Alloy 22 specimens. There were no aluminum precipitates on the non-creviced foils or pucks among the specimens exposed to vapor, however some silica from an unidentified source was detected. Figure 4.7 shows the Auger depth profiles of the atom percent of the alloy metals ($\text{Me}/(\text{Ni}+\text{Cr}+\text{Mo}+\text{W}+\text{Fe})$) and atom percent of Si and O as a function of sputter time. In contrast to the liquid-immersed specimens, silica and oxygen do not appear to be from the same phase as is seen in the varying Si:O ratio with depth (Figure 4.7b,d,f). Thus, oxygen should be associated with the alloy metals forming an oxide enriched in Ni and depleted in Cr and Mo relative to the base metal (Figure 4.7a,c,e). Almost equal concentrations of Cr and Mo are found in the surface layers; however, the concentrations are about half of those of Ni. Fe and W, which are present at very low concentration in the base metal, are barely detectable in the surface oxide layer. The depth profiles for the metal alloys show a distinct Ni-rich outer layer and a Cr-rich inner layer at sputter depths within 1 minute of the surface. This observation of compositionally distinct layers in the passive film has been observed for Alloy 22 at 25°C when corrosion was induced electrochemically at near neutral pH (Orme 2005).

In the absence of thick aluminum precipitates, we calculate the alloy oxide depth as the number of minutes needed to sputter to alloy ratio in the base metal (constant value in Figure 4.5a,c,e). In contrast to the liquid-immersed specimens, the alloy oxide thickness of 1 to 6 minutes (5.7 to 34.2 SiO_2 -equivalent nm) for the vapor phase specimens does not appear to depend strongly on temperature or the composition of the bulk brine solution.

The weight loss measurements are summarized in Figure 4.4 for vapor-exposed Alloy 22 foils. In contrast to the liquid-immersed specimens, all specimens showed a modest weight gain, indicating no contamination from the ceramic crevice formers and in agreement with the elemental depth profiles. Removal of oxides after 14 acid washes yielded near zero corrosion rates of 5 ± 11 nm/year (DTN LL050903312251.149).

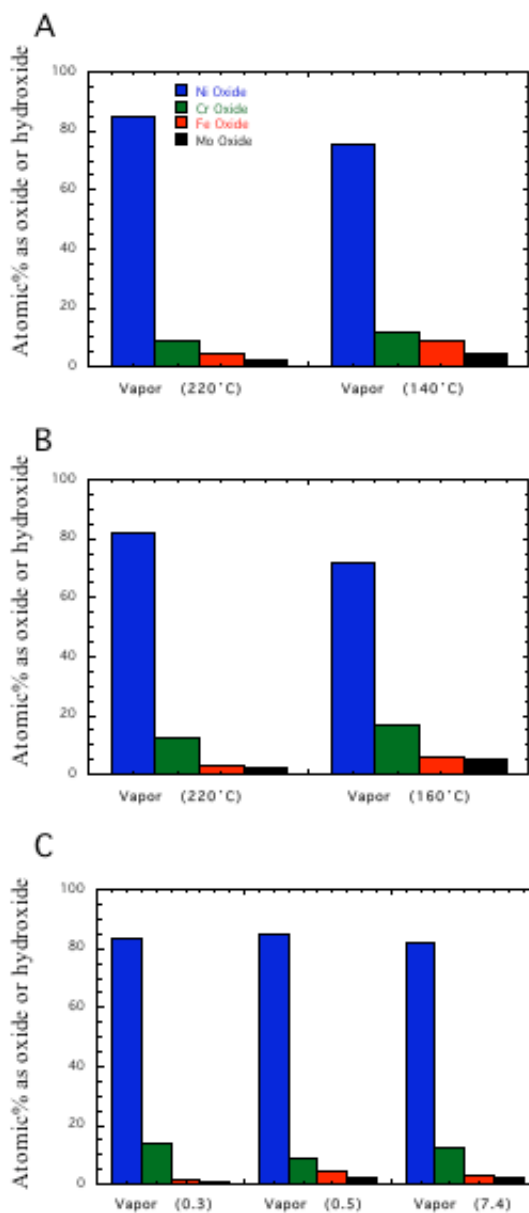


Figure 4.5 Comparison of atomic % of alloy metal ions as oxide or hydroxide determined by XPS as a function of temperature in solutions with $\text{NO}_3:\text{Cl} = 0.5$ (A) and $\text{NO}_3:\text{Cl} = 7.4$ (B); and as a function solution $\text{NO}_3:\text{Cl}$ at 220°C (C). Data for experiments at 140°C and 220°C at $\text{NO}_3:\text{Cl} = 0.3$ are from Orme et al., 2005. All other data are from this study.

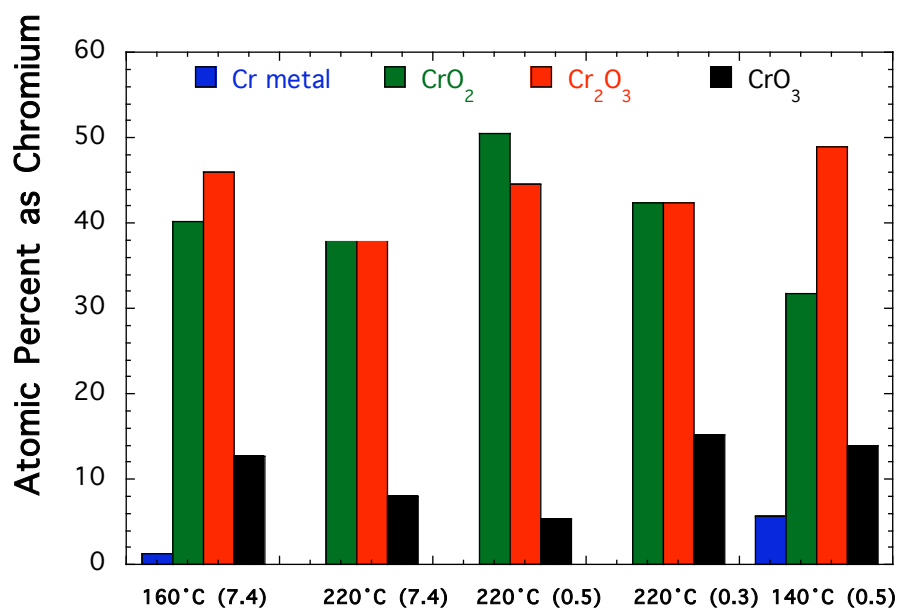


Figure 4.6. Chromium species distribution in the surface of vapor phase specimens aged for nine months in autoclaves at different temperature and in solutions containing different nitrate to chloride ratio (indicated in brackets). Data for experiments at 140°C (NO₃:Cl = 0.5) and 220°C (NO₃:Cl = 0.3) are from Orme et al., 2005. All other data are from this study.

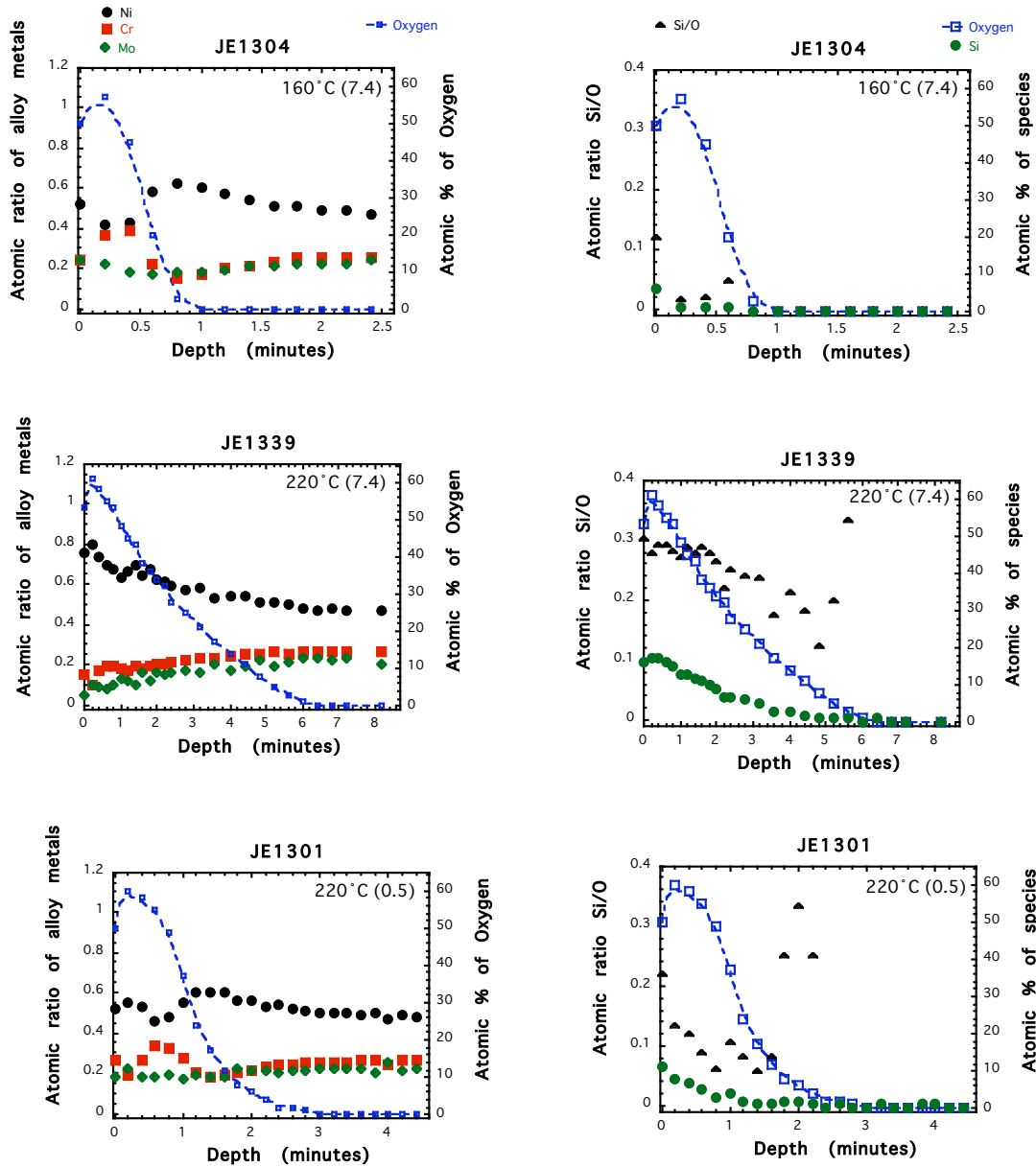


Figure 4.7: Auger depth profiles of vapor phase specimens autoclaved for nine months at 160 and 220°C at NO₃:Cl = 0.5 or 7.4 (ratio in parentheses). Note the different scales on the two y-axis of each of the plots.

5. Discussion

5.1. General Corrosion at High Temperature in High Nitrate Solutions

Slow dissolution kinetics of a Cr(III)-oxide passive film is believed to limit corrosion of Alloy 22 (Orme et al., 2005; Orme 2005). A Cr-rich inner oxide layer is present at the base metal surface in the vapor-exposed specimens and possibly in the liquid-immersed specimens (actual enrichment in Cr may be masked by less frequent analysis at longer sputtering times). While slow dissolution kinetics of a Cr-rich inner

layer may limit corrosion of Alloy 22 in the vapor phase where limited amounts of condensed water is the primary reactant, this may not be the case for Alloy 22 immersed in high nitrate brines at high temperatures. For the immersed specimens, it is reasonable to assume that growth of the aluminum hydroxide and of the alloy oxide occur concurrently. Thus the elemental depth profiles show a reaction front at the base metal, where oxidation produces a residual alloy oxide. A second reaction front occurs between the aluminum hydroxide precipitates and the dissolving alloy oxide. The depth profiles show that continued reaction of the alloy oxide leaches Cr and Mo, creating Ni-rich oxide relative to the base metal. This indicates that Cr and Mo oxides are more soluble than the Ni oxide, which would occur if Cr and Mo were oxidized to 6+ valence state oxy-anions. Thus younger oxide near the base metal has an alloy metal ratio that approximates the ratio in the base metal, and older oxides are enriched in Ni relative to Cr and Mo, because there has been more time to dissolve the Cr and Mo. This interpretation is supported by previous experiments at 220°C in Na-K-Cl-NO₃ brines with NO₃:Cl = 0.3. These experiments show that the Ni-enriched alloy oxide layer grows with increased reaction over 4 to 9 months, which implies that the base metal continues to corrode (Orme et al., 2005). The preferential dissolution of Mo and Cr relative to Ni over nine months suggests that when Alloy 22 is immersed in high nitrate brines at high temperatures Mo and Cr do not provide the same level of protection against corrosion compared to Alloy 22 in contact with limited amounts of water vapor.

5.2. Localized Corrosion

Crevice specimens were included with the general corrosion specimens⁶ to test the hypothesis that nitrate inhibits localized corrosion at high temperatures in brines with high NO₃:Cl ratios. Ratios of NO₃:Cl = 0.5 and 7.4 were thought to be high enough to inhibit localized corrosion at elevated temperature. The experimental conditions of this study differ from repository conditions in that they were conducted in a closed nitrogen-purged environment with about half of the specimens fully immersed in brines with NO₃:Cl = 0.5 and 7.4 at slight pressures to maintain solutions at 160 and 220°C (at atmospheric pressures the brines would have evaporated yielding dry salt mixtures at the experimental temperatures). Brines formed by the deliquescence of salts in the in-drift environment are expected to be thin films with NO₃:Cl > 25 at the upper end of expected temperatures (BSC 2005; Felker et al., 2006).

A single explanation for the cause of localized corrosion in both the vapor and immersed Alloy 22 specimens in these experiments cannot be evaluated from the limited test matrix of these multi-component experiments. In this section we summarize the current model for the initiation of localized corrosion of Alloy 22 and discuss the impact that experimental artifacts, temperature, and brine chemistry may have on the initiation of localized corrosion.

⁶ The autoclave experiments were initially set up in F04 to study general corrosion of Alloy 22 from 120 to 220°C as a function of time over a range of NO₃:Cl. Crevice samples were added to the FY05 experiments to study both general and localized corrosion at the same time.

5.2.1. Summary of waste package outer barrier localized corrosion model

Empirical evidence collected by the Yucca Mountain Project has shown that the initiation of localized corrosion of Alloy 22 is dependent on temperature, chloride and nitrate concentration, and the ratio of nitrate to chloride. The localized corrosion initiation model developed in *General Corrosion and Localized Corrosion of Waste Package Outer Barrier* (BSC, 2004b) is based on polarization tests to 120°C in which localized corrosion of Alloy 22 initiates when the steady-state corrosion potential (E_{corr}) is equal to or greater than the critical potential ($E_{critical}$). As a conservative measure, the localized corrosion initiation model uses the crevice repassivation potential (E_{rcrev}) as the critical potential. The functional form of the model is summarized below because it expresses the relationship between temperature, pH and brine chemistry.

The model is based on E_{corr} data from non-creviced Alloy 22 specimens immersed at a given temperature and brine chemistry for at least 328 days (~0.9 years), because long immersion times were necessary to obtain steady-state values for this parameter. The steady-state corrosion potential is best modeled as a function of temperature, pH, chloride and nitrate concentrations as follows:

$$E_{corr} = c_o + c_1T + c_2pH + c_3[Cl^-] + c_4 \log\left(\frac{[NO_3^-]}{[Cl^-]}\right) \quad (\text{Eq. 1})$$

where c_o , c_1 , c_2 , c_3 , and c_4 are empirical constants, T is temperature (°C), $[Cl^-]$ and $[NO_3^-]$ are the molal chloride and nitrate concentrations, respectively, and pH is calculated as the NBS pH using EQ3 and the Pitzer data base (Wolery and Jarek, 2003; BSC 2004b). The crevice repassivation potential is defined as follows:

$$E_{rcrev} = E_{rcrev}^o + \Delta E_{rcrev}^{NO_3^-} \quad (\text{Eq. 2})$$

where, E_{rcrev}^o is the crevice repassivation potential in the absence of nitrate ions and $\Delta E_{rcrev}^{NO_3^-}$ is the change in crevice repassivation potential from the inhibiting effect of nitrate ions. Crevice repassivation potentials are from polarization test data for creviced specimens that were immersed in a solution at temperature for about 24 hours. The crevice repassivation potential of the waste package outer barrier in the absence of nitrate is best modeled as a function of T, pH, and chloride concentration as follows:

$$E_{rcrev}^o = a_o + a_1T + a_2pH + a_3 \log([Cl^-]) + a_4T \times \log([Cl^-]) \quad (\text{Eq. 3})$$

where, a_o , a_1 , a_2 , a_3 , and a_4 are empirical constants. The effect of nitrate ion on the crevice repassivation potential ($\Delta E_{rcrev}^{NO_3^-}$) is best modeled as a function of nitrate concentration and nitrate to chloride ratio as follows:

$$\Delta E_{rcrev}^{NO_3^-} = b_o + b_1[NO_3^-] + b_2 \frac{[NO_3^-]}{[Cl^-]} \quad (\text{Eq. 4})$$

where, b_0 , b_1 and b_2 are empirical constants.

The use of equations 1- 4 to predict the initiation of localized corrosion is applicable only to temperatures below 120°C, because sufficient data were not available to extend the model over the full thermal range of the repository. At temperatures above 120°C, a conceptual model is used to predict the initiation of localized corrosion (BSC 2004c, Section 8.1). According to the conceptual model, no localized corrosion is initiated if solution NO₃:Cl ratio ≥ 0.5 when the temperature is greater than 120 °C and less than or equal to 160°C. At temperatures above 160°C, localized corrosion is initiated if water is present, regardless of the solution composition.

Comparison of the experimental results of this study and the conceptual model suggest that model be slightly modified so that at temperatures greater than or equal to 160°C (as compared to above 160°C), localized corrosion is initiated if water is present regardless of the nitrate to chloride ratio, because localized corrosion occurred on specimens exposed to condensates with estimated NO₃:Cl ratio = 0.5 and on specimens immersed in brines with a NO₃:Cl ratio = 0.5 and 7.4 (Table 3.2).

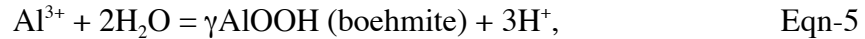
Accelerate short-term electrochemical tests can be used to describe the long-term performance of Alloy 22, because the metal-passive film-water interface is approximated by the use of steady-state E_{corr} values (Evans et al., 2006). Any change in the surface chemistry or the integrity of the passive film over geologic time should be in response to changes in the environment (i.e. temperature and solution composition). The use of the repassivation potential as the lower boundary for the initiation of localized corrosion also appears to be a robust parameter. Localized corrosion is initiated within 30 minutes when the potential is held above the repassivation potential (Yilmaz et al., 2005). However, comparison of localized corrosion observed in the 9-month autoclave experiments at 160°C in solutions with high nitrate to chloride ratios (Na-K brines, NO₃:Cl = 7.4 and NO₃ = 18.5 molal) with no localized corrosion of Alloy 22 at the same temperature in accelerated electrochemical tests with much lower nitrate to chloride (Ca brines, NO₃:Cl = 0.5 and NO₃ = 12 and 18 molal) (Ilevbare et al., 2006), indicate that electrochemical tests require longer exposure to capture localized corrosion in concentrated brines that form at higher temperature. Extension of the localized corrosion initiation model for Alloy 22 to high temperatures should be constrained by electrochemical data derived at multiple scan rates to ensure that transport of reactants does not mask electrochemical measurements.

5.2.2. Is localized corrosion an artifact of the experimental protocol?

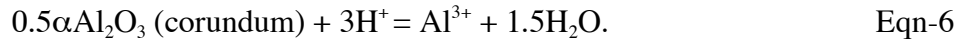
In this section we discuss the likelihood that pressure, mineral precipitation, cold work, and chromium depletion in as-received specimens caused localized corrosion of Alloy 22 in these experiments. It has been suggested that that the small pressure set by the partial pressure of water in these experiments may have compromised the passive film, presumably by pressure-induced dissolution, and contributed to the observed localized corrosion of Alloy 22 specimens. The geochemical community has routinely used nominal pressures to maintain dilute aqueous solutions at elevated temperature to study the dissolution kinetics and stability of oxides and silicates at elevated temperatures with no deleterious effects on reaction rate or mineral stability (Brantley and White, 1995; Carroll et al., 1998ab; Carroll and Knauss, 2005). Chromium oxide and chromium nickel

spinel are analog minerals for the Alloy 22 passive film and should not be compromised by the nominal pressures set by the partial pressure of water in this study.

It is unlikely that precipitation of secondary aluminum phases contribute to localized corrosion by increasing the acidity of the crevice solution, because any increased acidity by precipitation of boehmite (γ -AlOOH),



would be buffered by the dissolution of the aluminum oxide crevice former, the source material for the bulk of the secondary precipitates,



From a thermodynamic point of view, corundum (as well as a host of other aluminum oxides) will dissolve to form boehmite, because boehmite is the most stable phase at 160 and 220°C. The secondary precipitates probably formed over the duration of the experiment and not as the solution cooled to room temperature at the end of the experiment, because predicted dissolved aluminum concentrations are too small to generate the abundance of precipitates observed on the specimens (Table 3.2). The amount of aluminum hydroxide precipitation would be constrained by the dissolution kinetics of the aluminum oxide crevice former. Some of the aluminum hydroxide appear to have precipitated within the corrosion tracks (i.e. Figure 4.1c). It is possible that the precipitate forms an occluded environment in addition to the crevice former, but this can not be evaluated with the available data. In the crevice environment, dissolved aluminum has the potential to react with the passive film, however aluminum is not known to compromise the chromium rich passive film.

It has been suggested that deformation of the foil surface from the attachment of the crevice formers enhanced localized corrosion observed in this study. Deformation could result from crimping of the foils during attachment because the teeth of the crevice formers on top and underneath the foil may have been slightly offset. About 40 to 50% of the foils exhibited obvious deformation in the root of the crevice tooth due to attachment (or detachment) of the crevice former to (or from) the specimen. If cold work due to the obvious deformation were responsible for localized corrosion, then no localized corrosion should be observed on the non-deformed foils. However, localized corrosion was observed in all liquid-immersed and vapor-exposed creviced areas at all conditions of this study. If cold work were to explain localized corrosion, then it would have to result from more subtle deformation of the foil surface from the applied torque in the attachment process, presumably on the nanometer depth scale. Note that tightening crevice formers to 70 in-lb is a standard procedure for the study of localized corrosion by Yucca Mountain Project to create occluded environments. Similar amounts of cold work in the surface should occur regardless of the thickness of the specimen.

It has also been suggested that the use of as-received annealed foils may have enhanced the initiation of localized corrosion because the alloy surfaces may be depleted in chromium. Dunn et al. (1995) made the following observations on non-creviced Alloy 825 specimens: (1) Mill surface specimens were depleted in chromium relative to the

bulk metal, as identified by EDS (typically micron depths); (2) Localized corrosion initiated in cyclic potentiodynamic polarization tests on mill finished specimens only after the outer layers were uniformly dissolved; and (3) The application of constant potential above the repassivation potential yield localized corrosion in the mill finished specimens, but not in the polished specimens. They attribute the more reactive nature to chromium depletion in the alloy surface (a kind of de-alloying) and surface roughness. The effect chromium depletion of the alloy surface on localized corrosion has not been explicitly studied on Alloy 22, however comparison freshly polished and high temperature annealed (in air at 1121°C for 20 minutes and then water quenched) Alloy 22 specimens show similar resistance to localized corrosion (Rebak et al., 2006). The annealed specimens yielded a black-green film that was indicative of chromium oxide that forms at high temperature. These results indicate that any chromium depletion in the alloy surface due to the annealing process did not enhance localized corrosion of Alloy 22. Note also that foils are typically annealed in inert atmosphere (hydrogen gas) to minimize oxidation to preserve the thickness of the metal in the thin foil. This process will minimize the preferential depletion of chromium on the foil surfaces.

5.2.3. Role of nitrate on Alloy 22 localized corrosion at high temperature

Nitrate inhibition of localized corrosion of Alloy 22 has been systematically measured and captured in the Alloy 22 localized corrosion initiation model to temperatures less than 120°C (Section 5.2.1). Additional electrochemical studies in Ca-Cl-NO₃ brines to 160°C and K-Na-Cl-NO₃ brines to 150°C also report that nitrate inhibits localized corrosion of Alloy 22 (Ilevbare et al., 2006; Felker et al., 2006). Localized corrosion observed in the passive 9-month experiments suggests that NO₃:Cl ratios above 7.4 may be required to inhibit localized corrosion at 160 and 220°C. The observation that higher NO₃:Cl ratios are required at higher temperature is supported by other studies of Alloy 22 in Na-K-Cl-NO₃ brines. The critical value of NO₃:Cl increases from 0.05 to 0.2 from 60 to 90°C in a systematic study of the effect of NO₃:Cl ratios on Alloy 22 corrosion in simulated crevice solutions (Gray et al., 2005). At temperatures above 100°C, the amount of nitrate required to inhibit corrosion continues to increase. Felker et al. (2006) report localized corrosion on creviced Alloy 22 specimens from short-term cyclic potentiodynamic polarization tests at 110°C at NO₃:Cl = 1, but no localized corrosion was observed at 110, 125, 140, and 150°C in solutions with a NO₃:Cl ratio of 10.5, 10.5, 25.3, and 100 respectively (DTN: LL051001012251.154). Felker et al (2006) did not test lower NO₃:Cl ratios to determine critical values needed to inhibit localized corrosion in part because lower nitrate to chloride brines are not stable at the atmospheric testing conditions of their experiments. Note that defining temperature dependent NO₃:Cl ratios necessary to inhibit the initiation of localized corrosion should be used with caution, because systematic studies of nitrate inhibition in the Ca-Cl-NO₃ system from 100 to 150°C indicate that nitrate inhibition is dependent on the nitrate and chloride concentrations as well as the NO₃:Cl ratio (Ilevbare et al., 2006) in agreement with the Yucca Mountain model at temperatures less than 120°C (Section 5.2.1).

In addition to nitrates ability of inhibit localized corrosion, there is also evidence for nitrate oxidation of Alloy 22 and the Cr(III)-rich passive film. Gray et al., (2005) observed concurrent reduction of nitrate and oxidation of molybdenum to Mo(VI) on Alloy 22 at 60°C and acidic conditions using in-situ Raman spectroscopy. It is

reasonable to expect that chromium was also oxidized to Cr(VI) by nitrate, although it was not monitored by Raman spectroscopy. Indirect evidence of nitrate oxidation of a Cr(III)-rich passive film may be seen in the general corrosion specimens immersed in high nitrate brines (this study). Chromium and molybdenum are preferentially leached over nickel from the oxide layer of the liquid-immersed Alloy 22 pucks. Preferential leaching of chromium and molybdenum may be explained by the oxidation of the Cr(III) and Mo(II) in the alloy oxide by nitrate to form highly soluble Cr(VI) and Mo(VI) aqueous species. Enhanced dissolution of the passive film would result in additional corrosion of Alloy 22 to maintain steady-state thickness of the passive film. The role of nitrate as an oxidant is not a new idea. Thermodynamics predict that nitrate is an oxidant over thermal range that has been estimated for the repository. Concentrated nitric acid has long been used in industry to passivate metal surfaces. Formation of the protective passive film requires oxidation of the zero valent alloy.

Experimental observations that suggest nitrate both protects Alloy 22 against localized corrosion and contributes to Alloy 22 oxidation can be reconciled when one considers that processes that promote and inhibit corrosion occur concurrently and are kinetically controlled (Table 5.1). Generally, chloride ions promote localized corrosion and the extent of localized corrosion is enhanced with increasing temperature. Localized corrosion is then sustained by acid solutions resulting from hydrolysis of dissolved metals. Localized corrosion will also be enhanced at high temperature, because oxide dissolution kinetics generally increase with temperature, yielding a passive film that is less robust at higher temperature. The passive film may be further compromised by faster dissolution kinetics at acid pH and the oxidation Cr(III) in the passive film to highly soluble Cr(VI) by nitrate at higher temperature. Nitrate inhibition must then occur concurrently to counteract localized corrosion. Consider two mechanisms that are consistent with autoclave results. One mechanism calls on the reduction of nitrate in low pH corrosion pits or crevices (Frankel, 1998). Nitrate reduction consumes protons, raises the pH and lowers the likelihood for corrosion, because alloy dissolution rates are significantly lower at neutral pH. A second mechanism assumes that nitrate oxidizes chromium metal to produce a highly insoluble Cr₂O₃ passive film, which protects the alloy from further corrosion (Orme 2005, Orme et al., 2005).

Table 5.1. Processes contributing to localized corrosion of Alloy 22 in Na-K-Cl-NO₃ brines

Promotes Corrosion	Inhibits Corrosion
<ol style="list-style-type: none"> 1. Chloride attack of surface 2. Metal hydrolysis generates acid pH 3. Higher dissolution rates of the passive film at acid pH and higher temperature 4. Higher dissolution rates of passive film due to Cr(III) oxidation to Cr(VI)_{aq} (by nitrate in these experiments) 	<ol style="list-style-type: none"> 1. NO₃ oxidizes Cr metal to Cr(III)-rich passive film 2. NO₃ reduction at acid pH neutralizes solution and lowers corrosion and passive film dissolution rates

If we assume that nitrate inhibits localized corrosion by neutralizing pH and by forming a robust passive film, then higher nitrate concentrations will be needed to offset localized corrosion at higher temperature, because faster chloride-promoted corrosion will generate more acid, and because the protective passive film will need to be regenerated at a faster rate to compensate for faster oxide dissolution kinetics. In order to fully predict the dominant mechanism for a specific environment it is necessary to isolate and quantify each process as a function of temperature (which is not possible at this time). Localized corrosion observed on Alloy 22 specimens immersed in Na-K-Cl-NO₃ brines suggests that nitrate concentrations up to 18.5 molal are not sufficiently high to neutralize solution pH in the crevice environment due to chloride-promoted localized corrosion at 160°C and 220°C. The resulting acid pH further enhances corrosion by preventing the repassivation of Alloy 22. It is also possible, that rapid dissolution of the passive film at these high temperatures prevents repassivation of Alloy 22 regardless of the solution composition.

Localized corrosion observed on Alloy 22 specimens suspended in the vapor above the Na-K-Cl-NO₃ brines may be explained in part by the acid composition of the condensate in the crevice former. We assume that the vapor forms a condensate between the crevice former (individual teeth) and the Alloy 22 foil. The condensate is in equilibrium with the vapor, such that the calculated pH for the condensate reflects the partial pressures of HCl(g) and HNO₃(g). The calculated condensate pH ≈ 3 is fairly acidic compared to the brine pH ≈ 6 and may have initiated localized corrosion in the vapor-exposed specimens in these closed experiments (Table 3.2). Once initiated, localized corrosion may be sustained by increased acidity due to metal hydrolysis, because the crevice former does not appear to neutralize acid pH. Reaction of the condensate with the crevice formers did not have a significant effect on calculated brine or condensate pH and therefore could not have acted to drive localized corrosion.

6. Summary: Relevance of Autoclave Results to Corrosion of Alloy 22 in Dust Deliquescent Environments

We return to the decision tree from the *Analysis of Dust Deliquescence for FEP Screening* report (BSC 2005) to summarize the relevance of the autoclave experiments on the likelihood of localized corrosion of Alloy 22 in the repository:

1. Can multi-salt deliquescent brines form at elevated temperatures?
2. If brines form at elevated temperature, will they persist?
3. If brines persist, will they be corrosive?
4. If potentially corrosive brines form, will they initiate localized corrosion?
5. Once initiated, will localized corrosion penetrate the waste package outer barrier?

Specifically, this report addresses question 3 and 4 concerning the corrosiveness of Na-K-Cl-NO₃ brines and their ability to initiate localized corrosion. The autoclave results show that nitrogen-purged Na-K-Cl-NO₃ brines with up to 18.5 molal NO₃ and NO₃:Cl ratios as high as 7.4 are corrosive at 160°C and 220°C and will initiate localized corrosion in occluded environments and general corrosion on bold surfaces. Acid condensates

generated from $p\text{HCl}(\text{g})$ and $p\text{HNO}_3(\text{g})$ above the brines will also initiate localized corrosion in occluded environments and minimal amounts of general corrosion on bold surfaces. These statements are made with the caveat that additional tests are needed to fully rule out potential contributions from the experimental protocol. It is not known if more concentrated nitrate brines with NO_3 concentrations in excess of 100 molal and $\text{NO}_3:\text{Cl} > 25$ will be corrosive at peak temperatures associated with dust deliquescence. If they are corrosive it is possible that localized corrosion will be limited by transport processes in the very small amount of fluid available for corrosion. In an open system, such as the repository, it is not known if degassing will lead to dry out of the brines through chemical transformations. It is likely, that acid condensates generated from the vapor may be readily neutralized by calcite in the dust and drift wall; thus reducing corrosion of Alloy 22.

The observation of localized corrosion in creviced samples at elevated temperature suggest that the conceptual model be modified to show that localized corrosion is initiated at 160°C and above when water is present (as compared to above 160°C in the current model). Comparison of passive experiments to electrochemical experiments also suggest that extension of the localized corrosion initiation model for Alloy 22 to high temperatures should be constrained by electrochemical data derived at multiple scan rates to ensure that transport of reactants do not mask the initiation of localized corrosion.

Although, general corrosion occurs in the absence of occluded environments, it was not possible to determine reliable general corrosion rates from the weight-loss method. Despite the observation of thin and much thicker alloy oxide layers for the respective vapor-exposed and liquid-immersed specimens, the weight-loss method yielded near zero rates for both types of samples. Accurate measure of general corrosion rates from long-term passive tests requires the use of alternative methods to capture the durability of the Alloy 22, even at high temperature.

7. References

Brantley, S. and White, A. (1995) Chemical Weathering Rates of Silicate Minerals, *Reviews in Mineralogy*, **31**, 583p.

BSC (Bechtel SAIC Company) (2004a) Environment on the Surfaces of the Drip Shield and Waste Package Outer Barrier. ANL-EBS-MD-000001 REV 01. Las Vegas, Nevada.

BSC (Bechtel SAIC Company) (2004b). In-Drift Precipitates/Salts Model. ANL-EBS-MD-000045 REV 02. Las Vegas, Nevada: Bechtel SAIC Company.

BSC (Bechtel SAIC Company) (2004c). *General Corrosion and Localized Corrosion of Waste Package Outer Barrier*. ANL-EBS-MD-000003 REV 02. Las Vegas, Nevada: Bechtel SAIC Company. ACC: DOC.20041004.0001.

BSC (Bechtel SAIC Company) (2005) Analysis of Dust Deliquescence for FEP Screening. ANL-EBS-MD-000074 REV 00. Las Vegas, Nevada: Bechtel SAIC Company.

- Carroll-Webb S. A. and Walther J. V., (1988) A surface complex reaction model of the pH dependence of corundum and kaolinite dissolution rates. *Geochimica et Cosmochimica Acta*, **52**, 2609-2624.
- Carroll S. A., Mroczek E., Alai, M., Ebert M. (1998a) Amorphous silica precipitation (60° to 120°C): Comparison of laboratory and field rates. *Geochimica et Cosmochimica Acta* **62**, 1379-1396.
- Carroll S. A., Alai M., Bruton C. J. (1998b) Experimental investigation of cement, Topopah Spring tuff, and water interactions at 200°C. *Applied Geochemistry* **13**, 579-587.
- Carroll, S. A. and Knauss, K. G. (2005) Dependence of labradorite dissolution kinetics on CO₂(aq), Al(aq), and temperature. *Chemical Geology*, **217**, 213-225
- Carroll, A., Alai, M., Craig, L., Gdowski, G., Hailey, P., Nguyen, G., Rard, J., Staggs, K., Sutton, M., Wolery, T. (2005a) Chemical Environment at Waste Package Surfaces in a High-Level Radioactive Waste Repository, Lawrence Livermore National Laboratory, UCRL-TR-212566.
- Carroll, A., Rard, J., Staggs, K., Wolery, T. Alai, M., (2005b) Brines formed by multi-salt deliquescence, Lawrence Livermore National Laboratory, UCRL-TR-217062.
- Dunn, D. S., Sridhar, N., and Cragolino, G. A. (1995) Effects of surface chromium depletion on localized corrosion of Alloy 825 as a high-level nuclear waste container material. *Corrosion* **51**, 618-624
- Deer, W. A., Howie, R. A., and Zussman, J. (1992) An Introduction to the Rock-Forming Minerals. Longman Scientific and Technical p. 496-515.
- Evans, J. K., Stuart, M. L., Etien, R. A., Hust, G. A., Estill, J. C., Rebak, R. (2006) Long-term corrosion of potential and corrosion rate of creviced Alloy 22 in chloride plus nitrate brines. Corrosion NACEExpo. Paper No. 06623.
- Felker, S., Hailey, P., Lian, T., Staggs, K., Gdowski, G. (2006) Alloy 22 localized corrosion susceptibility in aqueous solutions of chloride and nitrate salts of sodium and potassium at 110 - 160°C. Lawrence Livermore National Laboratory, UCRL-TR-2198195.
- Frankel, G. S.(1995) Pitting Corrosion of Metals: A Review of the Critical Factors. J. Electrochem. Soc., 145, 2186-2199.
- Gray J. J., Hayes, J. R., Gdowski, G. E., Orme, C. A. (2005) Inhibiting effects of nitrates on the passive film breakdown of alloy 22 in chloride solutions. J. Electrochem. Soc., accepted.

Gordon, G. M. (2002) Corrosion considerations related to permanent disposal of high-level radioactive waste. *Corrosion*, **58**, 811-825.

Ilevbare, G. O. King, K. J., Gordon, S. R., Elayat, H. A., Gdowski, G. E., and Gdowski, T.S.E (2005) Effect of nitrate on the repassivation potential of Alloy 22 in chloride-containing environments, *J. Electrochemical Soc.*, 152, B547-554.

Ilevbare, G. O., Estill, J. C., Yilmas, A., Etien, R. A., Hust, G. A., Stuart, M. L., and Rebak, R. B. (2006) Anodic behavior of Alloy 22 in high nitrate brines at temperature higher than 100C. *ASME Pressure Vessels and Piping Division Conference Proceeding*, in press.

Orme, C., Gray, J., Hayes, J., Wong, L., Rebak, R., Carroll, S., Harper, J., Gdowski, G. (2005) General Corrosion and Passive Film Stability: FY04 Summary Report. Lawrence Livermore National Laboratory, UCRL-TR-208588.

Orme, C. (2005) Passive Film Report. Lawrence Livermore National Laboratory, UCRL-TR-215277.

Pitzer, K. S., 1991. Ion interaction approach: Theory and data correlation. In: K. S. Pitzer, (Editor) Activity Coefficients in Electrolyte Solutions, 2nd. Ed, CRC Press: Boca Raton, FL, pp. 75–153.

Rebak, R. (2000) Corrosion of Non-ferrous Alloys. I Nickel-, Cobalt-, Copper-, Zirconium- and Titanium Based Alloys, in *Materials Science and Technology - A Comprehensive Treatment* (eds. Chan, Haasen, Kramer), Vol. 19, *Corrosion and Environmental Degradation*, (M. Schütze editor), Vol II, Chapter 2, 69-111.

Rebak, R. B., Etien, R. A., Gordon S. R., Ilevbare, G. O. (2006) Influence of black annealing oxide scale on the anodic behavior of Alloy 22. *Corrosion NACEExpo* (in press)

Weast, R. C. and Astle, M. J. (1981) CRC Handbook of Chemistry and Physics. CRC Press Inc., p. D-169.

Wolery, T. J. and Jarek, R. L., 2003. EQ3/6, Version 8.0, Software User's Manual, Software Document Number: 10813-UM-8.0-00, U.S. Department of Energy, Office of Civilian Radioactive Waste Management, Office of Repository Development, 1261 Town Center Drive, Las Vegas, Nevada 89144.

Yilmas, A., Pasupahti, P., Rebak, R. B. (2005) Stifling of crevice corrosion in Alloy 22 during constant potential tests. *ASME Pressure Vessels and Piping Division Conference Proceeding*.

8. Appendix: Long-term Corrosion Test Facility

Table 7.1 shows the status of experiments in the Long-Term Corrosion Test Facility. Additional FY05 activities included the development of an inventory system for the more than 19,000 metals specimens. About 3000 metal specimens still need to be placed in the inventory. Additional specimens were acid cleaned for weight loss analysis of burnished, laser peened, as-welded, and heat-to-heat variability specimens (DTN: LL050600812251.146 and LL050502512251.145.). Two scientific notebooks are under review (SN241v3 and SN483v1). Tanks #1-8 and 16 were never purchased.

Table 7.1: Status of experiments in the Long-Term Corrosion Test Facility.

Vessel #	Vessel Start Date	Solution Type	Temperature	Materials In Test
9	9/25/97	SCW	60° C	Carbon steel coupled to Ni-based & Ti-based materials
10	9/25/97	SCW	90° C	Carbon steel coupled to Ni-based & Ti-based materials
11	9/25/97	SCW	60° C	Copper-Nickel & Monel
12	9/25/97	SCW	90° C	Copper-Nickel & Monel
13	9/24/97	SDW	60° C	Copper-Nickel & Monel
14	9/24/97	SDW	90° C	Copper-Nickel & Monel
15	Empty	Empty	120° C	Empty
17	8/8/97	SDW	60° C	Carbon steel coupled to Ni-based & Ti-based materials
18	9/18/97	SCMW	90° C	Carbon steel coupled to Ni-based & Ti-based materials
19	9/17/97	SCMW	60° C	Carbon steel coupled to Ni-based & Ti-based materials
20	11/15/96	SCW	90° C	Carbon & Low Alloy Steel
21	10/28/96	SCW	60° C	Carbon & Low Alloy Steel
22	10/10/96	SDW	90° C	Carbon & Low Alloy Steel plus Ceramic Coated Carbon Steel
23	9/24/96	SDW	60° C	Carbon & Low Alloy Steel
24	8/8/97	SDW	90° C	Carbon steel coupled to Ni-based & Ti-based materials
25	2/6/97	SAW	60° C	Nickel Based Alloys & Titanium (825, G3,625, C-4, C-22, Ti Gr 12, 16, 7)
26	2/21/97	SAW	90° C	Nickel Based Alloys & Titanium (825, G3,625, C-4, C-22, Ti Gr 12, 16, 7)
27	3/10/97	SCW	60° C	Nickel Based Alloys & Titanium (825, G3,625, C-4, C-22, Ti Gr 12, 16, 7)
28	4/10/97	SCW	90° C	Nickel Based Alloys & Titanium (825, G3,625, C-4, C-22, Ti Gr 12, 16, 7)
29	4/14/97	SDW	60° C	Nickel Based Alloys & Titanium (825, G3,625, C-4, C-22, Ti Gr 12, 16, 7)
30	4/17/97	SDW	90° C	Nickel Based Alloys & Titanium

				(825, G3,625, C-4, C-22, Ti Gr 12, 16, 7)
31	Empty	DI H2O	60° C	DI H2O
32	Empty	DI H2O	90° C	DI H2O
33	9/22/97	SCMW	60° C	Carbon Steel
34	9/22/97	SCMW	90° C	Carbon Steel
35	Empty	Empty	120° C	Empty
36	Empty	Empty	120° C	Empty
37	Empty	Empty	120° C	Empty